iScience

CellPress
OPEN ACCESS

Article

Clustering in ferronematics—The effect of magnetic collective ordering

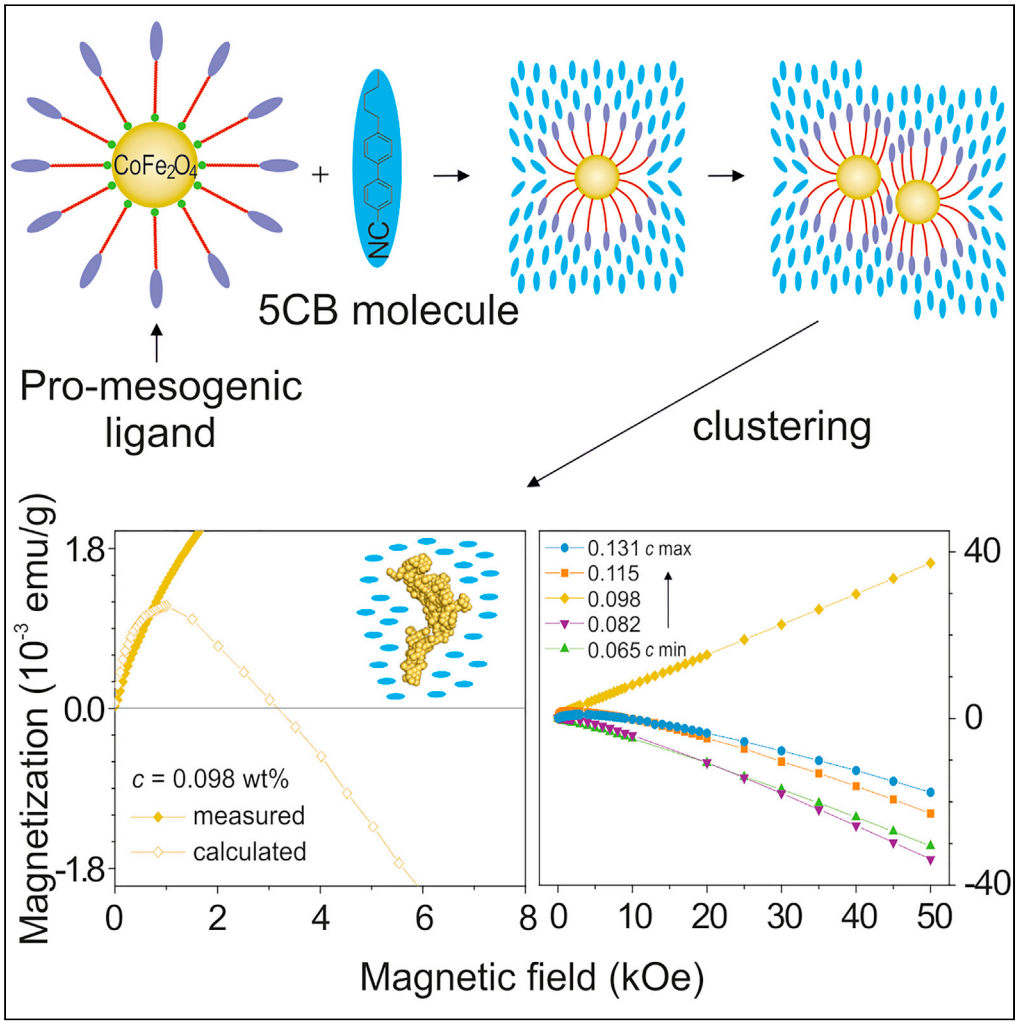

Veronika Lacková, Martin A. Schroer, Dirk Honecker, ..., Dmitri I. Svergun, Peter Kopčanský, Natália Tomašovičová

nhudak@saske.sk

Highlights

Modification of nanoparticle surfaces with specific ligands

Combined experimental approach reveals structure and magnetization

Clustering of magnetic nanoparticles in a liquid crystal matrix

Cluster form dramatically changes collective magnetic properties

Lacková et al., iScience 24, 103493
December 17, 2021
https://doi.org/10.1016/j.isci.2021.103493

iScience

CellPress
OPEN ACCESS

Article

Clustering in ferronematics—The effect of magnetic collective ordering

Veronika Lacková,[1] Martin A. Schroer,[2,3] Dirk Honecker,[4] Martin Hähsler,[5,6] Hana Vargová,[1] Katarína Zakutanská,[1] Silke Behrens,[5,6] Jozef Kováč,[1] Dmitri I. Svergun,[2] Peter Kopčanský,[1] and Natália Tomašovičová[1,7,*]

SUMMARY

Clustering of magnetic nanoparticles can dramatically change their collective magnetic properties, and it consequently may influence their performance in biomedical and technological applications. Owing to tailored surface modification of magnetic particles such composites represent stable systems. Here, we report ferronematic mixtures that contain anisotropic clusters of mesogen-hybridized cobalt ferrite nanoparticles dispersed in liquid crystal host studied by different experimental methods—magnetization measurements, small-angle X-ray scattering (SAXS), small-angle neutron scattering (SANS), and capacitance measurements. These measurements reveal non-monotonic dependencies of magnetization curves and the Fréedericksz transition on the magnetic nanoparticles concentration. This can be explained by the formation of clusters, whose structures were determined by SAXS measurements. Complementary to the magnetization measurements, SANS measurements of the samples were performed for different magnetic field strengths to obtain information on the orientation of the liquid crystal molecules. We demonstrated that such hybrid materials offer new avenues for tunable materials.

INTRODUCTION

The revolutionary improvements in nanomaterial preparation and control of properties for nanometer-scale structures enable the development of new products, applications, as well as technologies, e.g., in medical and high-tech devices (Kumar et al., 2013; Jeevanandam et al., 2018; Andrews et al., 2019). Very attractive from the designing point of view as functional nanomaterials, liquid crystal-based nanocomposites can be aligned or reoriented by external stimuli such as temperature, light, magnetic, and/or electric fields. Lately, combining the unique properties of nanoparticles (NPs) with the anisotropy of liquid crystals (LCs) has opened up new opportunities for tuning the properties of LCs for novel materials that contribute to the nanotechnology revolution, mainly in areas such as sensors, nanoscale electronics, electro-optics, optical memories, and display devices (Hegmann et al., 2007; Stamatoiu et al., 2012). In 1970, Brochard and de Gennes theoretically predicted interesting ferronematic (FN) properties for ferrofluids of LCs doped with anisotropic magnetic nanoparticles (MNPs) (Brochard and de Gennes, 1970). Since then, the hybridization of LCs and NPs has produced new materials in which the response to external stimuli has been dramatically increased. For instance, a low concentration of ferroelectric NPs in different LC media (Copic et al., 2007; Kaczmarek et al., 2008; Liang et al., 2010; Gupta et al., 2010) enhanced birefringence as well as a larger dielectric anisotropy was observed. Moreover, such suspensions showed a reduced Fréedericksz threshold voltage (Reshetnyak et al., 2006) and faster response time in comparison with pure nematic hosts. Besides, in-plane switching for nematic LC was found to be faster after doping with monolayers of graphene flakes (Basu et al., 2016). A lot of interest has been devoted to carbon nanotubes that have an impact on LCs electro-optical properties (Chen et al., 2007; Basu et al., 2010, 2011; Petrov et al., 2013). Other studies on LC systems doped with quantum dots have shown the possibility to modify the dielectric, electro-optical properties of LCs as well as the pitch of cholesteric LCs (Kumar et al., 2011; Cho et al., 2014; Rodarte et al., 2012, 2014; Patranabish et al., 2021; Han et al., 2021).

In analogy with the aforementioned observations, the question naturally arises, if doping with magnetic particles could lead to unique unexpected global magnetic properties of novel mixed compounds. An exhaustive analysis in this field as well as the deeper understanding of relevant driven mechanisms will

[1]Institute of Experimental Physics, Slovak Academy of Sciences, Watsonová 47, 04001 Košice, Slovakia

[2]European Molecular Biology Laboratory, Hamburg Outstation c/o DESY, Notkestr. 85, 22607 Hamburg, Germany

[3]Nanoparticle Process Technology University of Duisburg-Essen, Lotharstr. 1, 47057 Duisburg, Germany

[4]Institut Laue-Langevin, 71 Avenue des Martyrs, 38042 Grenoble, France

[5]Institut für Katalyseforschung und -technologie, Karlsruher Institut für Technologie, Postfach 3640, 76021 Karlsruhe, Germany

[6]Anorganisch-Chemisches Institut, Universität Heidelberg, Universität Heidelberg, Im Neuenheimer Feld 270, 69120 Heidelberg, Germany

[7]Lead contact

*Correspondence: nhudak@saske.sk

https://doi.org/10.1016/j.isci.2021.103493

be very valuable owing to the huge application potential of MNPs-doped LCs, e.g., in displays, drug delivery vehicles, sensors, or optical elements as controllable lens and lasing, data storage, medical imaging, and in microwave devices (Bahadur, 1990; Lagerwall and Scalia, 2012; Prakash et al., 2020). Creating such hybrid systems, commonly referred to as ferronematics (FNs), demands for long-term stability, which is achieved for highly diluted systems with rather low concentrations of MNPs ($10^{-3} - 10^{-4}$ wt%) (Tóth-Katona et al., 2014; Prodanov et al., 2016; Qi et al., 2009). Moreover, size and surface properties of MNPs are essential factors for their stabilization in such hybrid materials (Saliba et al., 2013). Therefore, various surfactants are extensively studied for coating the MNP's surface to decrease or avoid aggregation of MNPs and improve the long-time stability (Podoliak et al., 2012). Recent studies have elaborated specific surface engineering of MNPs with (pro-) mesogenic ligands to prepare NP-LC hybrids and tuning their compatibility with thermotropic LC hosts (Demortiére et al., 2010; Appel et al., 2017; Gdovinová et al., 2017; Hähsler et al., 2021). The stability of colloids crucially determines the structure-property relationships and future applications. In our previous work we have studied the changes in the LC structure of a simple nematic mesogen caused by doping with mesogen-hybridized $CoFe_2O_4$-MNPs as well as the influence of phase transition on the colloidal stability, especially on the alignment of MNPs (Gdovinová et al., 2017). The choice of this specific MNP was motivated by its wide range of interesting properties like the high chemical stability, mechanical hardness, high coercivity, moderate saturation magnetization, and large magnetocrystalline anisotropy (Hashim et al., 2012; Sanpo et al., 2013; Momin et al., 2015; Sharifi et al., 2012; Hähsler et al., 2020; Zákutná et al., 2020), which allow us to expect an unconventional macroscopic behavior of MNP-doped LCs. Indeed, the obtained results in Gdovinová et al. (2017) showed a rapid change in magnetization for a concentrated FN sample contrary to its diluted counterpart in which the influence of MNPs is negligible in comparison with the undoped LC. The observed different behavior of FN samples based on an identical LC and doped with the same kind of MNPs suggests that it is possible to change the magnetic properties of such hybrid dramatically by changing the weight concentration of MNPs in the LC host. In the present paper, we therefore investigated in detail the response of MNPs-doped nematic LC host (4-n-pentyl-4′-cyanobiphenyl (5CB)) to an applied magnetic field over a wide weight concentration range of MNPs. In order to stabilize the $CoFe_{0.6}O_{2.4}$-MNPs (CFO-MNPs) in the LC host, the CFO-MNPs were functionalized with a promesogenic ligand (i.e., [16-((4′-cyano-[1,1′-biphenyl9-4-yl)oxy)hexadecanoic acid]) to yield CFO@ligand-MNPs. To perform a systematic analysis the suspensions of 5CB doped with CFO@ligand-MNPs were prepared with five different concentrations: LC1, 0.065 wt.%; LC2, 0.082 wt.%; LC3, 0.098 wt.%; LC4, 0.115 wt.%; and LC5, 0.131 wt.%. We observed a non-trivial magnetic behavior. For all FN mixtures, the study combines SQUID magnetometry and complementary capacitance measurements, small-angle X-ray and neutron scattering measurements to investigate the structural transition and alignment of MNPs and LC.

RESULTS AND DISCUSSION

Before a detailed discussion we would like to note that differences in the thermal regime of all used experimental methods (capacitance, SQUID, SANS, and SAXS measurements) do not have any significant impact on the qualitative interpretation of the obtained results. All mentioned measurements were done in nematic state of LC, i.e., below the isotropic-nematic transition temperature. The aforementioned statement is in particular based on the SAXS thermal analysis (exhaustively described in the Supporting Information), where the averaged scattering intensity as well as the orientational order parameter are almost thermally independent for all five investigated samples in the temperature range below 30°C.

Magnetization measurements

The magnetization measurements performed on the SQUID magnetometer are presented in Figure 1. At first, it was necessary to verify the magnetic response of both colloidal components separately to better understand the behavior of their mixture. In accordance with our expectation, the shape of the magnetization curve of $CoFe_{0.6}O_{2.4}$ (CFO-MNPs) powder presented in Figure 1A reflects the magnetic properties of CFO-MNPs with a typical "S" behavior. The size of the MNP-core is below the Shliomis size (Fortin et al., 2007; Hergt et al., 2010) and therefore the magnetic moment relaxes due to Néel relaxation. In Figure 1B the magnetization curve of undoped 5CB is given indicating diamagnetic behavior characterized through the linear behavior of magnetization with a negative slope at high-enough amplitude of an external magnetic field.

The most interesting results of our investigation are collected in Figure 2, where the response of MNPs-doped LC on an applied magnetic field is presented for all five concentrations: LC1, 0.065 wt.%; LC2. 0.082 wt.%; LC3, 0.098 wt.%; LC4, 0.115 wt.%; and LC5, 0.131 wt.%. Apparently, the magnetization curve behavior is non-trivial,

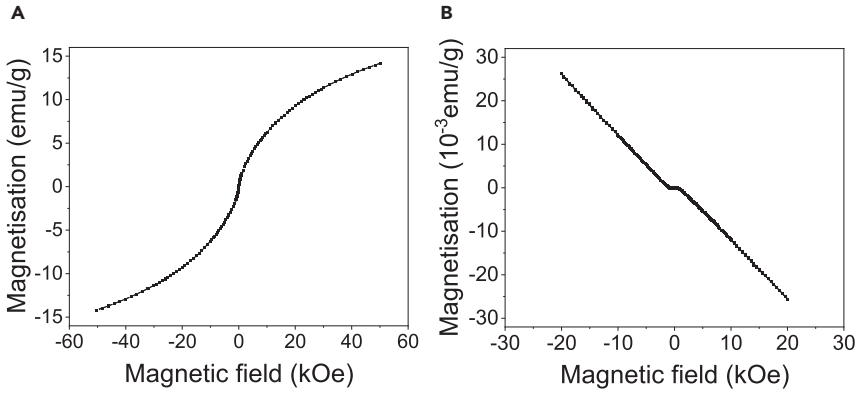

Figure 1. The magnetization curves

(A and B) (A) CFO-powder and (B) undoped 5CB liquid crystal measured at T = 295 K (~22°C).

the increase of MNPs concentration does not lead to a proportionate increment of the saturation magnetization. For a weak magnetic field (see Figure 2B), the highest magnetic response of analyzed systems is detected for the LC4 compound, whereas the magnetization of the most concentrated sample LC5 is detected significantly below the LC4 and even the LC3 sample. One possible explanation of this unexpected behavior could be a modified total magnetic moment due to the relevant changes of dipolar magnetic interaction among the particles. We suppose that the increasing collinear magnetic interparticle coupling supports the effect of an external magnetic field, resulting in the rapid increment of magnetization in comparison with a disordered system. On the other hand, anticorrelation between neighboring core moments (Bender et al., 2018) hamper an external magnetic field to reorient all magnetic moments in its direction, and thus the final magnetization curve is observed below its paramagnetic counterpart.

For comparison, we calculated the magnetization curves for well dispersed, non-interacting MNP in LC medium, shown in Figure 3. In such colloid, both components, ferromagnetic from MNPs and diamagnetic from LC, contribute to final magnetization (Saari et al., 2015). The comparative analyses of experimental measurement and calculations are shown in Figure 4.

The experimentally measured magnetic moments of the LC2 and LC5 compounds do not achieve the saturation value of their non-interacting counterparts contrary to the sample LC4, where the measured magnetic response is obviously above the theoretical predictions indicating an antiferromagnetic and ferromagnetic type of interaction, respectively. An extreme behavior is detected for the samples LC1 and LC3. LC1 shows a purely dominant diamagnetic contribution of the LC in the final magnetic curve. In contrast to this, the diamagnetic contribution originating from the LC matrix in the LC3 sample is completely reduced and an almost perfect linear character of measured curve is observed in the whole investigated region of an applied electric field. The strong, unexpected deviation of the saturation magnetization of all samples hints to strong connection between MNP aggregates and nematic direction. Strongly anisotropic MNPs structures could potentially overcome entropic effects that usually dominate the orientation behavior of liquid crystals and could be interpreted as an enhancement of a magnetic anisotropy in the sample as a consequence of a strongly anisotropic type of MNPs clusters.

All observations discussed apparently suggest the existence of different types of the magnetic exchange interaction in the colloids under the variation of MNPs concentration. We suppose that the driving mechanism responsible for such unexpected behavior could be found in the formation of different magnetic clusters in CFO-LC at the specific concentration of MNPs (Demortiére et al., 2010; Gdovinová et al., 2017). As shown by Clime and Veres (2007), the magnetization of densely packed interacting superparamagnetic nanoparticles assembled into clusters can increase or decrease compared with non-interacting particles, depending on the size and dimensionality of clusters.

SAXS measurements

To confirm our hypothesis, we have performed SAXS measurements to determine the structure of MNPs in the FN mixture at T= 40°C. At this temperature, the entire sample is isotropic, and, therefore, the

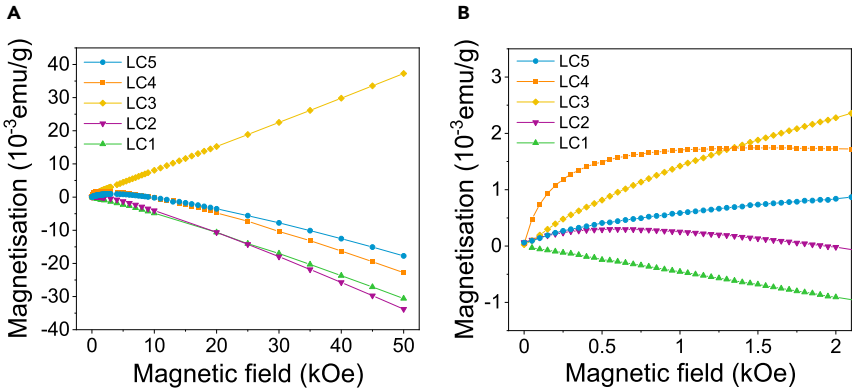

Figure 2. The magnetization curves of ferronematics

(A and B) (A) FN mixtures in the nematic phase for five different concentrations of MNPs over the whole investigated region of magnetic field and (B) at a low magnetic field.

corresponding 1D curves can be analyzed using standard approaches (Svergun et al., 2013; Li et al., 2016; Schroer and Svergun, 2018). As 5CB is unstructured under these conditions, it can be treated as an additional background contribution and subtracted from the 1D profiles of the mixtures. The corresponding background-corrected SAXS curves for MNPs at the five different concentrations are shown in Figure 5.

All curves exhibit similar angular dependency, which can be divided into three regions: at the smallest angles, for q<0.3 nm^{-1} the data exhibit a power law decay, whereas at wider angles, for q>1.0 nm^{-1} the profiles point to the presence of smaller particles. In the intermediate transition region, a shoulder due to interparticle correlations between the CFO@ligand-MNPs is observed. In more detail, for q> 1.0 nm^{-1} the absence of any form factor oscillation in the scattering profiles point to the lack of a distinct spherical particle shape and may indicate a polydisperse particle ensemble with size and shape dispersity.

The underlying volume weighted particle size distribution function $D_{Vol}(r)$ assuming spherical particles was determined from the outer parts of the SAXS curves (1.0 nm^{-1} <q<2.5 nm^{-1}) using the program GNOM (Svergun, 1992). The resulting distributions for all concentrations display a similar bimodal appearance with maxima at $r \approx 1.7$ nm and $r \approx 2.7$ nm (see Figure 6A). The observed deviations between the distributions are relatively minor and, in particular for $w = 0.065$ wt.% (LC1), are likely due to the limited accessible q-range for the determination of the distribution function (see the GNOM fit in Figure 5, which extrapolates the scattering signal to zero angles). The size of the MNPs core is $d = 3.1$ ($\pm$0.8) nm as determined by transmission electron microscopy. As the scattering contrast of the soft and flexible organic shell is much weaker than that of the MNPs, only the core is visible in the SAXS measurement (Schulz et al., 2018).

In the mid-q-range, 0.4 nm^{-1} <q<1.0 nm^{-1}, there is a strong deviation from the form factor contribution of the small MNPs, indicating the presence of interparticle interference. The rough position of the shoulder at q_{corr} is marked in Figure 5. The corresponding correlation length, estimated as $d_{corr} = 2\pi/q_{corr} \approx 7$ nm, only slightly exceeds the effective particle diameter (SAXS: ~4–6 nm) indicating that the particles are in rather close contact and interact with each other.

For q<0.3 nm^{-1}, the SAXS curves follow basically a power law decay, i.e., $I(q) \sim q^{-P}$ (Figure 5) with the power law exponent $p = 2.5$ at $c = 0.065$ wt.% and $p = 2.3$ for the other concentrations. Such a scattering curve is similar to that from mass-fractals and different from spherical and isometric particles (with $p = 4$) (Beaucage, 1996). Our data therefore point to the presence of reaction-limited clusters formed by the small MNPs in solution. Within these clusters, the MNPs are in close contact. A close inspection of the SAXS curves at small q actually indicates slight modulations of the power-law decay. In order to extract this additional structural information on the clusters, pair-distance distribution functions $p(r)$ from the SAXS profiles at very small q were determined. The results in Figure 6B indicate that the effective size of the clusters is indeed different, with a maximum size of at least d_{max} ~190 nm. In addition, the related shape of the clusters appears also to be different. Except for $c = 0.098$ wt.% (LC3) and, to a much lesser extent for $c = 0.082$ wt.% (LC2), the $p(r)$ functions demonstrate an inverted parabolic profile, typical for a flattened shape of the clusters. The $p(r)$ for LC3 points to an elongated shape of presented clusters.

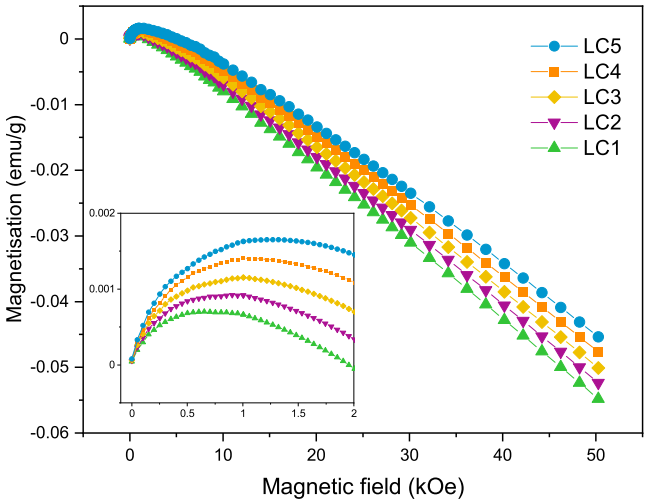

Figure 3. Calculated magnetization curves for well dispersed, non-interacting magnetic nanoparticles (MNPs) in liquid crystal (LC) medium

The curves were constructed for 1 g of mixture. The magnetization of composites was obtained by adding the contribution of the amount of LC and the amount of MNPs present in the composite (insert shows detail).

In order to obtain tentative shape models of the clusters, *ab initio* modeling from the SAXS curves at small angles has been performed using the program DAMMIN (Svergun, 1999) of the ATSAS package.

Figure 7 depicts the resulting *ab initio* shape models. As size of the dummy beads used to model the SAXS curves, a radius of 3 nm was chosen, which roughly corresponds to the MNP size. For all five samples, the models exhibit an overall elongated shape for the magnetic clusters. The models can be roughly separated into two classes: LC1, LC4, and LC5 have a more bulky and flat shape, whereas LC2 and, in particular, LC3 are much slimmer. All five models indicate a rather partially branched structure than a well-defined surface, indicative of the aggregation process. Also, all models exhibit an aspect ratio (AR) between 2 and 3. It should be noted that the presented models, owing to the size polydispersity as well as the aggregation process, represent an averaged cluster volume rather than a well-defined shape.

The asymmetric shape of all clusters can alternatively be directly deduced from the anisotropic shape of the 2D SAXS patterns, as is presented for one representative LC4 sample in Figure S1 of supplemental information. The scattering signal at small angles, stemming from the clusters, is aligned with respect to the 5CB matrix. In more detail, the short axis of these elongated clusters is pointing toward the LC director, indicating an orientational coupling between the LC matrix and MNP clusters. The different shapes of the clusters are expected to be a consequence of the (de-)aggregation process, which is dependent on the interparticle interactions, particle concentrations, and external perturbations, the last being induced by the dilution process (Mackert et al., 2021). As samples LC1 to LC4 have been prepared by dilution of the LC5 stock solution, the structural difference can be attributed to de- (LC3, LC4) and re-agglomeration (LC1, LC2) of structure LC5. LC4 exhibits a rather slightly different shape, indicative of mild disruptive effects, whereas LC3 appears to be broken up during the dilution process. On further dilution, the shapes become compact again, indicating re-aggregation. Therefore, the LC3 structure appears to reflect a rather stable structure, as further dilution did not result in additional fragmentation. As such a stability is dependent on the specific interactions between the nanoparticles forming the cluster, it appears reasonable that these interactions also have a particular influence on the response to external magnetic fields and thus are the reason for the observed findings.

SANS measurements

To provide independent confirmation of the results from the magnetization measurements, SANS measurements of the samples were performed at six different values of magnetic field (B = 0, 0.05, 0.1, 0.2, 0.5, and 1 T). SANS measurements with a polarized neutron beam (SANSPOL) in general allow one to obtain information on the magnetization distribution (Bonini et al., 2007). However, the data show

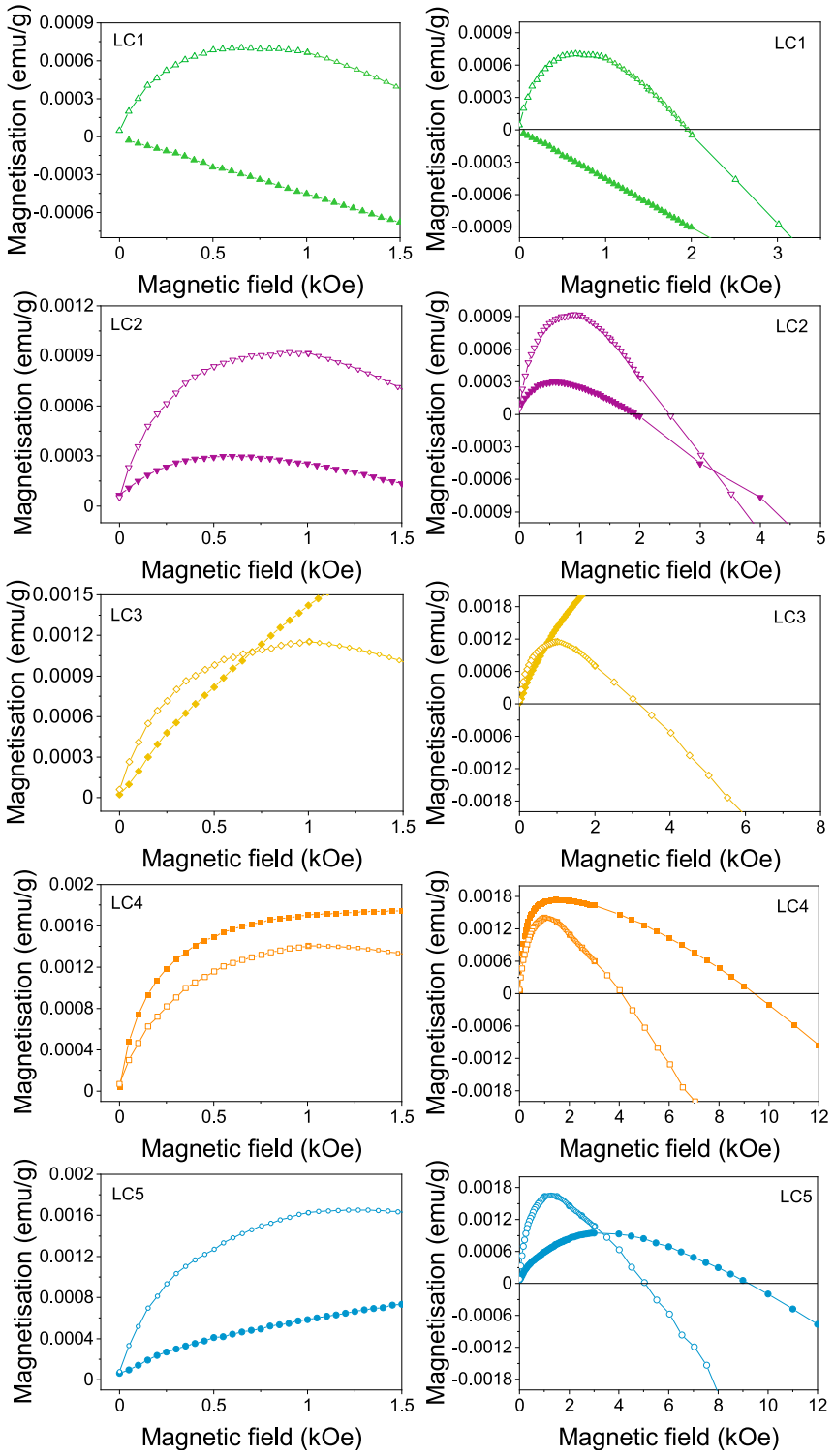

Figure 4. The comparative analysis of magnetizations curves

Full symbols represents calculated magnetization curves of the non-interacting MNP in LC medium. Open symbols represent measured magnetization of five investigated concentrations. The right panels are the details in the proximity of low magnetic field curves H<1.5 kOe.

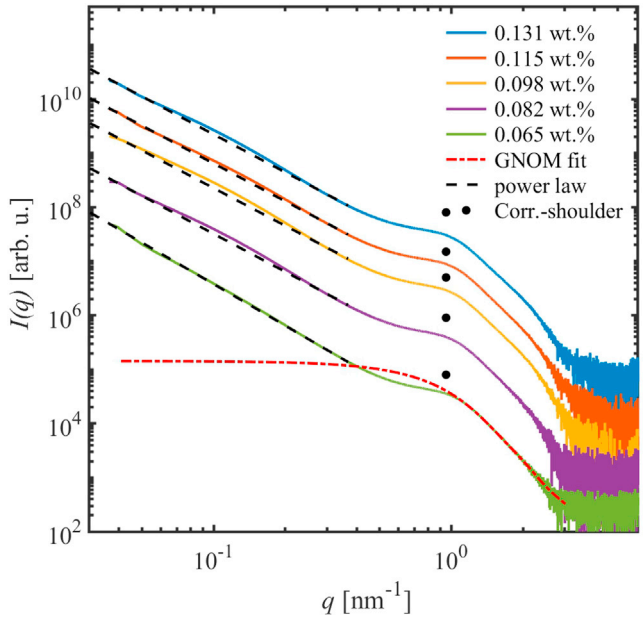

Figure 5. SAXS curves of FNs

A representative fitting curve from a distribution of spherical particles (GNOM fit for q<1 nm^{-1}) is also displayed for the whole q-range. At small q<0.3 nm^{-1}, power laws are fitted to the data. The positions of a shoulder due to interparticle correlations for each curve are marked by dots. The datasets are displaced along the intensity scale for clarity.

negligible spin-dependent nuclear-magnetic scattering cross sections in the per mille range compared with the total scattering. This finding is explained by the low volume fraction of MNPs such that the magnetic scattering due to MNPs is superimposed by the strong nuclear scattering of the LC host and the incoherent scattering background due to abundant hydrogen. The further analysis of the LC orientation was performed using the unpolarized SANS data.

For the undoped 5CB, a nearly isotropic scattering pattern is observed at zero applied magnetic field (Figure 8A). With applied magnetic field, one observes a transition to an elongated anisotropy with enhanced scattering along the (horizontal) field direction and reduced intensity in the vertical direction, due to an alignment of anisometric molecules perpendicular to the field; see Figure 8B.

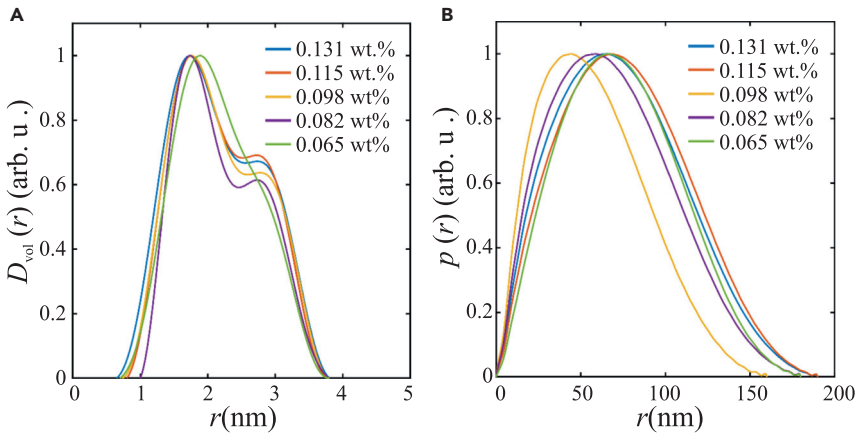

Figure 6. Distribution functions determined from the SAXS data

(A) Volume-weighted distribution $D_{Vol}(r)$ of the smaller MNPs.

(B) Pair-distance distribution function $p(r)$ for the large anisotropic clusters formed by the MNPs.

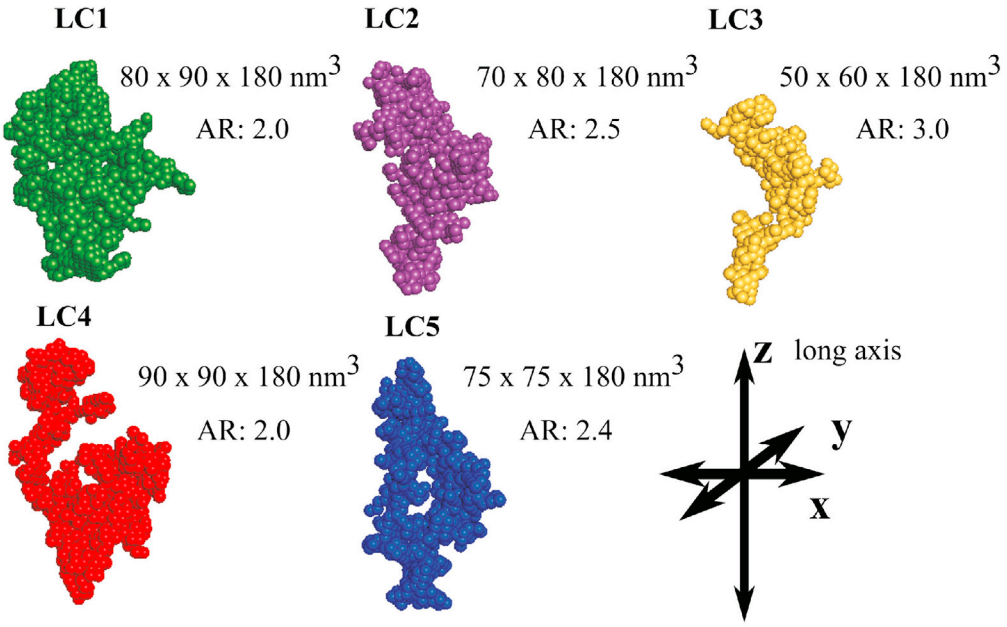

Figure 7. Shape models of the clusters determined from the SAXS curves

Within the 5CB matrix, the clusters are aligned such that their long axis are perpendicular to the nematic director. Given are also the average dimensions and the aspect ratio (AR).

However, for the FN mixtures, the scattering patterns initially show a fully different behavior depending on the MNPs concentration. In accordance with the SQUID measurements, we have identified three types of SANS patterns, collected in the left panel of Figure 9. The first one (Figures 9A and 9C), corresponding to the LC1 and LC2 samples, is characterized by an enhancement of intensity at the left upper and right lower corners, interpreted as magnetic liquid domains oriented perpendicular to each other.

The scattering of LC4 (Figure 9G) is characterized by the initially scattering pattern with the highest intensity in the right upper and left lower corners. The LC3 and LC5 mixtures are (Figures 9E and 9I) characterized by the strong scattering peak at B = 0 T, which rotates gradually perpendicular to the applied magnetic field direction (along the q_x vector). Consequently, already the various SANS patterns at B = 0 T show that there is a more or less strong prealignment of the LC. Since the external stimulus is identical for all investigated samples, we believe that the MNPs concentration is a crucial mechanism, which forms an initial magnetic arrangement. On analysis of the SANS patterns at non-zero magnetic field (see Figures S8–S12) one identifies different magnetic responses depending on the MNPs concentration. For an illustration see the right panel of Figure 9, which represents the SANS patterns at B = 0.1 T. It is clearly evident that the most anisotropic SANS intensity at B = 0.1 T corresponds to the LC3 sample, which hints to the larger magnetic

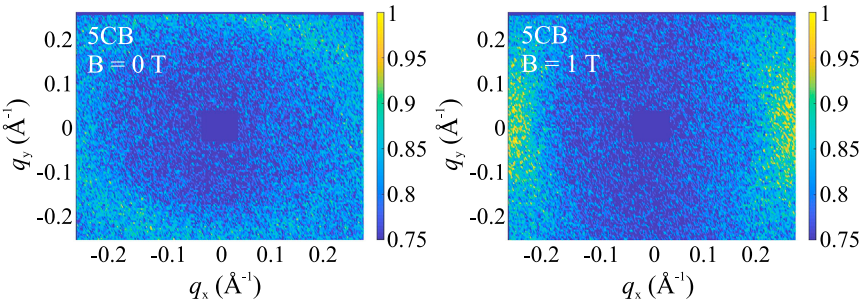

Figure 8. Two-dimensional SANS patterns

5CB without applied magnetic field and with B = 1 T at room temperature (T = 25°C). The magnetic field is oriented horizontal parallel to the q_x axis.

See also Figures S8–S12.

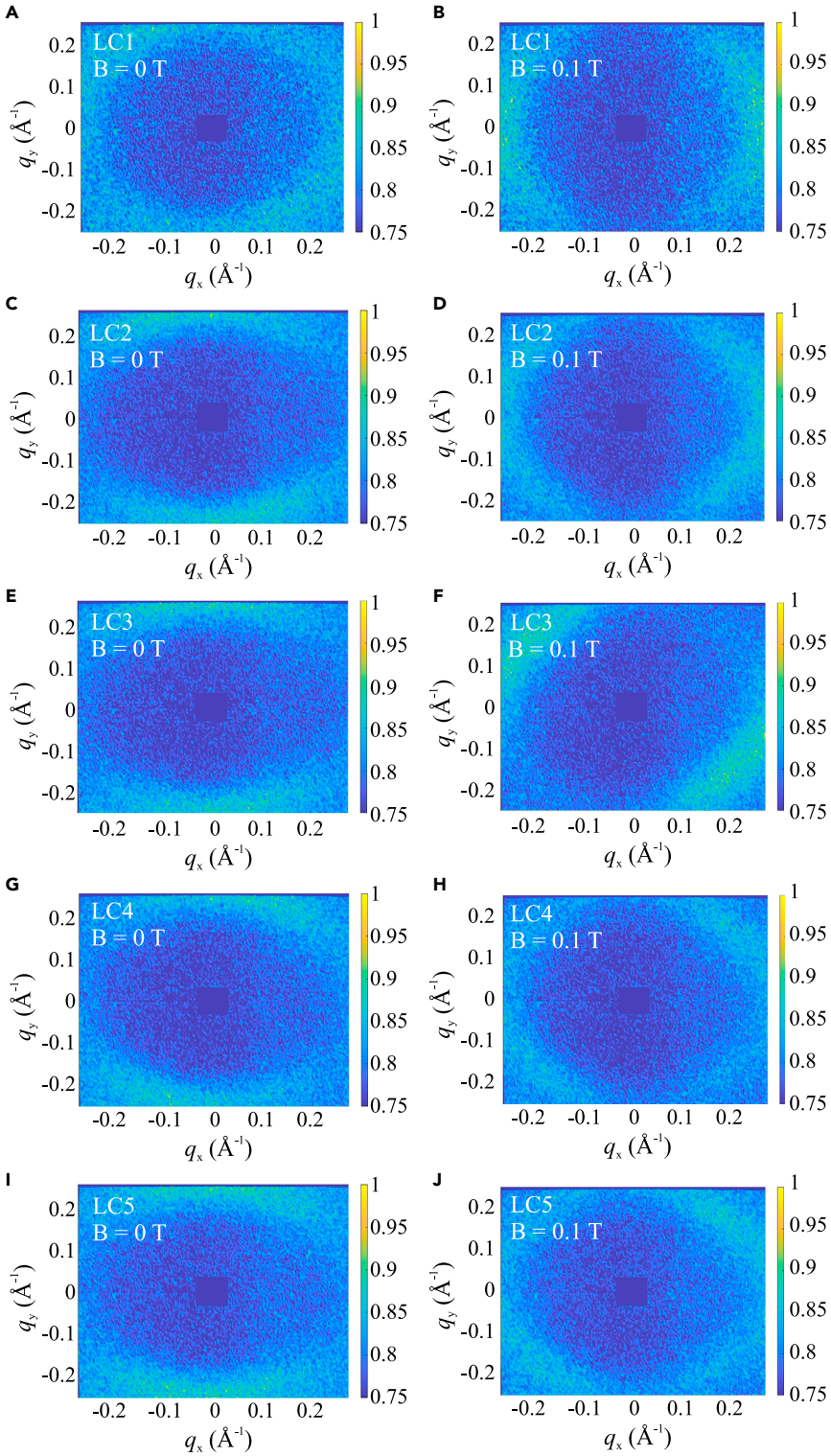

Figure 9. SANS scattering patterns measured at B = 0 T and B = 0.1 T

(A and B) LC1.

(C and D) LC2.

(E and F) LC3.

(G and H) LC4.

(I and J) LC5.

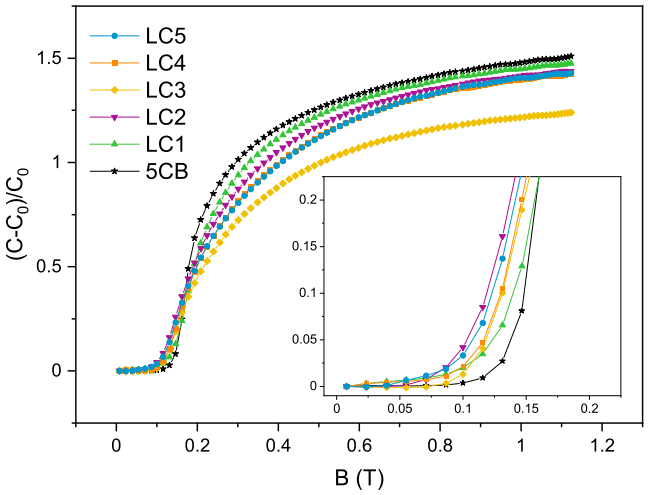

Figure 10. Magnetic Fréedericksz transition

Dependence of the capacitance of the LC 5CB and of the FNs on the applied magnetic field. Inset shows low field region.

susceptibility of the LC composite. In addition, the transition fields above which the scattering pattern is oriented along the vertical field varies with the MNPs concentration as a consequence of different correlations between magnetic particles and their response to magnetic field, and interactions of the MNP within the LC matrix. One observes for LC1 and LC3 a strong variation with moderate magnetic field of 0.1 T. For LC1, the scattering pattern indicates an almost aligned state, whereas for LC3 the system is still reorienting coherently at an intermediate orientation. For the other concentrations the onset of reorientation happens at fields of 0.2 T for LC2 and even larger for the other compositions. Two-dimensional SANS scattering patterns indicate that the fully polarized state is achieved more easily in the LC mixture with "more isotropic" magnetic clusters, instead of the highly anisotropic shape of the one observed, e.g., in the LC3 phase. For LC3, the scattering patterns at non-zero magnetic field indicate that the director rotates coherently for the whole sample (Figure S10 in the supplemental information). The other mixtures show a redistribution of scattering intensity that is along the field direction toward the edges of the detector for intermediate fields at 0.05–0.1 T caused by the rotation of tilted twin domains.

Capacitance measurements

Finally, we have analyzed the influence of MNPs clustering on the magnetic Fréedericksz transition. Figure 10 shows the capacitance measurements up to 1.2 T with magnetic field dependence of the reduced capacitance $(C - C_0)/C_0$ for undoped LC 5CB as well as for FN samples with different CFO@ligand-MNPs concentrations. Here C and C_0 correspond to the capacitances at the actual field and at B = 0 T, respectively. For the doped systems, the sensitivity increases with increasing dopant concentration, demonstrating that the magnetic Fréedericksz transition threshold is shifted toward lower fields, and thus from the application perspective gives an opportunity to prepare low-energy-consuming materials for FN applications. However, with increasing concentration of NPs in the composites, we would expect a monotonic decrease of the Fréedericksz transition threshold provoked by the magnetic field, but the obtained results show a non-monotonic behavior. Similarly as in the previous discussion, the concentration and arrangement of MNPs dopants and their properties (e.g., the shape and the effective size of magnetic clusters and/or the type of exchange interaction) have a non-negligible impact on the occurrence of the Fréedericksz transition threshold. It can be attributed to a strong magneto-nematic coupling in the system by choosing appropriate surface-attached MNPs to nematic media.

In conclusion, combining capacitance, magnetization, and SAXS and SANS measurements we present a description of composites made of cobalt ferrite NPs in the nematic LC host 5CB. The magnetic-field magnetization measurements of five concentration compounds (between 0.065 and 0.131 wt.%) performed on the SQUID magnetometer reveal the peculiar and unexpected behavior with a non-proportional enhancement of magnetization with MNPs concentration in colloid. Surprisingly, we identified the huge magnetic response at the MNPs concentration of 0.098 wt.%, in which the diamagnetic contribution is completely absent in the range of investigated magnetic field. On the other hand, the magnetic response

of the highest concentrated sample studied (0.131 wt.%) in a low-enough magnetic field is significantly smaller in comparison with other investigated concentrations. Based on the comparative analysis of the measured magnetization curves and theoretically predicted behavior of non-interacting MNPs in LC medium, we suppose that such unexpected observation of magnetic behavior relates to the dramatic changes of the effective correlation inside the LC suspension. For concentrations where the measured magnetization curves are above (below) the theoretical predictions, ferromagnetic (antiferromagnetic) correlation support (reduce) the effect of an external magnetic field. In accordance with this prediction, a high-enough effective correlation can completely overcome the diamagnetic contribution as is observed for LC3. On the contrary, effectively non-magnetic clusters cannot generate a sufficient magnetic response and, thus, the solely diamagnetic contribution is measured. The field-dependent SANS measurements from 0 to 1 T support our hypothesis. Already the 2D SANS patterns show for the MNP concentrations that different field strengths induce a transition from the initial orientation to the field-aligned state. In particular for LC3 a strong scattering anisotropy associated to enhanced orientational order is observed, in good correspondence with the outstanding magnetic response of this sample. It should be emphasized that the initial scattering patterns (B = 0 T) of all five analyzed samples do not coincide as a result of different spontaneous structural arrangements of the LC host. The obtained results suggest that variation of MNPs in the LC host can lead to the cluster formation, the size and dimensionality of which have an impact on global magnetic properties. Finally, from the SAXS we identified the presence of clusters in each analyzed sample. The morphology of these clusters is similar to mass-fractals formed by reaction-limited elongated clusters with an aspect ratio between 2 and 3. We demonstrate that the MNPs clusters induce a ferronematic response of the liquid crystal matrix with a rich concentration dependence. The clusters are coupled with the 5CB matrix. Within the nematic phase, the short axis is oriented toward the 5CB director.

Limitations of the study

Although our study, combing several experimental methods, revealed that the presence of clusters can create new types of hybrid material with new physical properties, the full mechanisms on the microscopic scale are not yet fully clear. Therefore, we expect our results will stimulate future experimental and theoretical work to reveal the underlying molecular mechanisms in detail. Further research will elucidate the way for fabricating stable ferronematics with tunable magnetic properties suitable for application such as magnetic field sensors or magneto-optical devices.

SUPPORTING CITATIONS

The following references appear in the supplemental information: Davidson et al. (1995); Lorenz et al., (2012); Silva et al., (2015).

STAR★METHODS

Detailed methods are provided in the online version of this paper and include the following:

- KEY RESOURCES TABLE
- RESOURCE AVAILABILITY
  - Lead contact
  - Materials availability
  - Data and code availability
- METHOD DETAILS
  - Synthesis of electrostatically stabilized CFO-MNPs
  - Synthesis of CFO@ligand-MNPs *via* direct functionalization
  - Preparation of FN mixtures: Doping 5CB with CFO@ligand-MNPs
  - Magnetisation measurements
  - Small angle X-ray scattering
  - Small angle neutron scattering
  - Dielectric measurements

SUPPLEMENTAL INFORMATION

Supplemental information can be found online at https://doi.org/10.1016/j.isci.2021.103493.

ACKNOWLEDGMENTS

The authors thank the support by the Slovak Academy of Sciences, in the framework of projects VEGA 2/0043/21 and VEGA 1/0105/20, the Slovak Research and Development Agency under the contract No. APVV-015-0453, MODEX (ITMS2014+:313011T548) supported by the Operational Programme Integrated Infrastructure (OPII) funded by the ERDF and COST action CA15119 Nanouptake. We gratefully acknowledge the financial support and provision of beam time at the instrument D33 at the Institut Laue-Langevin, Grenoble, France project No. 9-11-1883. M.A.S. and D.I.S. acknowledge the Roentgen-Angstroem cluster project "TT-SAS" (BMBF project number 05K16YEA) for financial support. S.B. and M.H. thank the German Science Foundation (DFG) for financial support within the Priority Program (SPP1681) "Field controlled particle matrix interactions. Synthesis, multiscale modeling, and application of magnetic hybrid materials" (project BE 2243/2-3).

AUTHOR CONTRIBUTIONS

V.L. conceptualization, investigation, writing draft; M.A.S. and D.I.S. SAXS investigation; D.H. SANS investigation; M.H. synthesis of samples; H.V. validation; K.Z. visualization; S.B. conceptualization of sample synthesis; J.K. magnetic properties investigation; P.K. funding acquisition; N.T. supervision; M.A.S., N.T., and D.H. writing, review and editing. All authors discussed the results and read and approved the final manuscript.

DECLARATION OF INTERESTS

The authors declare no competing interests.

Received: August 17, 2021
Revised: November 5, 2021
Accepted: November 19, 2021
Published: December 17, 2021

REFERENCES

Andrews, D., Nann, T., and Lipson, R. (2019). Comprehensive Nanoscience and Nanotechnology, Second Edition (Academic Press).

Appel, I., Nádasi, H., Reitz, C., Sebastián, N., Hahn, H., Eremin, A., Stannarius, R., and Behrens, S.S. (2017). Doping of nematic cyanobiphenyl liquid crystals with mesogen-hybridized magnetic nanoaprticles. Phys. Chem. Chem. Phys. *19*, 12127–12135. https://doi.org/10.1039/C7CP01438D.

Bahadur, B.E. (1990). Liquid Crystals-Applications and Uses (World Scientific), pp. 1–3.

Basu, R., Boccuzzi, K.A., Ferjani, S., and Rosenblatt, C. (2010). Carbon nanotube-induced chirality in an achiral liquid crystal. Appl. Phys. Lett. *97*, 121908. https://doi.org/10.1063/1.3492844.

Basu, R., Chen, C.-L., and Rosenblatt, C. (2011). Carbon nanotube-induced macroscopic helical twist in an achiral nematic liquid crystal. J. Appl. Phys. *109*, 083518. https://doi.org/10.1063/1.3576101.

Basu, R., Kinnamon, D., Skaggs, N., and Womack, J. (2016). Faster in-plane switching and reduced rotational viscosity characteristics in a graphene-nematic suspension. J. Appl. Phys. *119*, 185107. https://doi.org/10.1063/1.4949481.

Beaucage, G. (1996). Small-angle scattering from polymeric mass fractals of arbitrary mass-fractal dimension. J. Appl. Cryst. *29*, 134–146. https://doi.org/10.1107/S0021889895011605.

Bender, P., Wetterskog, E., Honecker, D., Fock, J., Frandsen, C., Moerland, C., Bogart, L.K., Posth, O., Szczerba, W., Gavilán, H., et al. (2018). Dipolar-coupled moment correlations in clusters of magnetic nanoparticles. Phys. Rev. B *98*, 224420. https://doi.org/10.1103/PhysRevB.98.224420.

Blanchet, C.E., Spilotros, A., Schwemmer, F., Graewert, M.A., Kikhney, A.G., Jeffries, C.M., Franke, D., Mark, D., Zengerle, R., Cipriani, F., et al. (2015). Versatile sample environments and automation for biological solution X-ray scattering experiments at the P12 beamline (PETRA iii, DESY). J. Appl. Cryst. *48*, 431–443. https://doi.org/10.1107/S160057671500254X.

Bonini, M., Wiedenmann, A., and Baglioni, P. (2007). Study of ferrite ferrofluids by small-angle scattering of polarized neutrons. J. Appl. Cryst. *40*, s254–s258. https://doi.org/10.1107/S0021889807009600.

Brochard, F., and de Gennes, P.G. (1970). Theory of magnetic suspensions in liquid crystals. J. Phys. (Paris) *31*, 691–708. https://doi.org/10.1051/jphys:01970003107069100.

Chen, H.-Y., Lee, W., and Clark, N.A. (2007). Faster electro-optical response characteristics of a carbon-nanotube-nematic suspension. Appl. Phys. Lett. *90*, 033510. https://doi.org/10.1063/1.2432294.

Cho, M.-J., Park, H.-G., Jeong, H.-C., Lee, J.-W., Jung, Y.H., Kim, D.-H., Kim, J.-H., Lee, J.-W., and Seo, D.-S. (2014). Superior fast switching of liquid crystal devices using graphene quantum dots. Liq. Cryst. *41*, 761–767. https://doi.org/10.1080/02678292.2014.889233.

Clime, L., and Veres, T. (2007). Numerical micromagnetics of interacting superparamagnetic nanoparticles assembled in clusters with different dimensionalities. J. Magn. Magn. Mater. *314*, 11–15. https://doi.org/10.1016/j.jmmm.2007.02.055.

Copic, M., Mertelj, A., Buchnev, O., and Reznikov, Y. (2007). Coupled director and polarization fluctuations in suspensions of ferroelectric nanoparticles in nematic liquid crystals. Phys. Rev. E *76*, 011702. https://doi.org/10.1103/PhysRevE.76.011702.

Davidson, P., Petermann, D., and Levelut, A.M. (1995). The measurement of the nematic order parameter by X-ray scattering reconsidereds. J. Phys. *5*, 113–131. https://doi.org/10.1051/jp2:1995117.

Demortiére, A., Buathong, S., Pichon, B.P., Panissod, P., Guillon, D., Bégin-Colin, S., and Donnio, B. (2010). Nematic-like organization of magnetic mesogen-hybridized nanoparticles. Small *6*, 1341–1346. https://doi.org/10.1002/smll.201000285.

Dewhurst, C.D., Grillo, I., Honecker, D., Bonnaud, M., Jacques, M., Amrouni, C., Perillo-Marcone, A., Manzin, G., and Cubitt, R. (2016). The small-

angle neutron scattering instrument D33 at the Institut Laue-Langevin. J. Appl. Crystallogr. *49*, 1–14. https://doi.org/10.1107/S1600576715021792.

Fortin, J.P., Wilhelm, C., Servais, J., Ménager, C., Bacri, J.C., and Gazeau, F. (2007). Size-sorted anionic iron oxide nanomagnets as colloidal mediators for magnetic hyperthermia. J. Am. Chem. Soc. *129*, 2628–2635. https://doi.org/10.1021/ja067457e.

Franke, D., Kikhney, A.G., and Svergun, D.I. (2012). Automated acquisition and analysis of small angle X-ray scattering data. Nucl. Instrum. Methods Phys. Rev. A *689*, 52–59. https://doi.org/10.1016/j.nima.2012.06.008.

Franke, D., Petoukhov, M.V., Konarev, P.V., Panjkovich, A., Tuukkanen, A., Mertens, H.D.T., Kikhney, A.G., Hajizadeh, N.R., Franklin, J.M., Jeffries, C.M., et al. (2017). Atsas 2.8: a comprehensive data analysis suite for small-angle scattering from macromolecular solutions. J. Appl. Cryst. *50*, 1212–1225. https://doi.org/10.1107/S1600576717007786.

Gdovinová, V., Schroer, M.A., Tomašovičová, N., Appel, I., Behrens, S., Majorošová, J., Kováč, J., Svergun, D.I., and Kopčanský, P. (2017). Structuralization of magnetic nanoparticles in 5CB liquid crystals. Soft Matter *13*, 7890–7896. https://doi.org/10.1039/c7sm01234a.

Gupta, M., Satpathy, I., Roy, A., and Pratibha, R. (2010). Nanoparticle induced director distortion and disorder in liquid crystal-nanoparticle dispersions. J. Colloid Interf. Sci. *352*, 292–298. https://doi.org/10.1016/j.jcis.2010.08.027.

Hähsler, M., Landers, J., Nowack, T., Salamon, S., Zimmermann, M., Heiß ler, S., Wende, H., and Behrens, S. (2020). Magnetic properties and Mössbauer spectroscopy of Fe^{3} O^{4}/$CoFe^{2}o^{4}$ nanorods. Inorg. Chem. *59*, 3677–3685. https://doi.org/10.1021/acs.inorgchem.9b03267.

Hähsler, M., Nádasi, H., Feneberg, M., Marino, S., Giesselmann, F., Behrens, S., and Eremin, A. (2021). Magnetic tilting in nematic liquid crystals driven by self-assembly. Adv. Funct. Mater. 2101847. https://doi.org/10.1002/adfm.202101847.

Han, Y., Harris, J., Walton, J., and Majundar, A. (2021). Tailored nematic and magnetization profiles on two-dimensional polygons. Phys. Rev. E *103*, 052702. https://doi.org/10.1103/PhysRevE.103.052702.

Hashim, M., Kumar, S., Koo, B.H., Shirsath, S.E., Mohammed, E.M., Shah, J., Kotnala, R.K., Choi, H.K., Chung, H., and Kumar, R. (2012). Structural, electrical and magnetic properties of Co-Cu ferrite nanoparticles. J. Alloys Compd. *518*, 11–18. https://doi.org/10.1016/j.jallcom.2011.12.017.

Hegmann, T., Qi, H., and Marx, V.M. (2007). Nanoparticles in liquid crystals: synthesis, self-assembly, defect formation and potential applications. J. Inorg. Organomet. Polym. Mater. *17*, 483–508. https://doi.org/10.1007/s10904-007-9140-5.

Hergt, R., Dutz, S., and Zeisberger, M. (2010). Validity limits of the Néel relaxation model of magnetic nanoparticles for hyperthermia. Nanotechnology *21*, 015706. https://doi.org/10.1088/0957-4484/21/1/015706.

Jeevanandam, J., Barhoum, A., Chan, Y.S., Dufresne, A., and Danquah, M.K. (2018). Review on nanoaprticles and nanostrucured materials: history, sources, toxicity and regulations. Beilstein J. Nanotechnol. *9*, 1050–1074. https://doi.org/10.3762/bjnano.9.98.

Kaczmarek, K., Buchnev, O., and Nandhakumar, I. (2008). Ferroelectric nanoparticles in low refractive index liquid crystals for strong electro-optic response. Appl. Phys. Lett. *92*, 103307. https://doi.org/10.1063/1.2884186.

Kraft, P., Bergamaschi, A., Broennimann, C., Dinapoli, R., Eikenberry, E.F., Henrich, B., Johnson, I., Mozzanica, A., Schleputz, C.M., Willmott, P.R., et al. (2009). Performance of single-photon-counting PILATUS detector modules. Performance of single-photon-counting PILATUS detector modules. J. Synchrotron Rad. *16*, 368–375. https://doi.org/10.1107/S0909049509009911.

Kumar, A., Chen, F., Mozhi, A., Zhang, X., Xue, X., Hao, Y., Zhang, X., Wang, P.C., and Liang, X.-J. (2013). Innovative pharmaceutical development based on unique properties of nanoscale delivery formulation. Nanoscale *5*, 8307–8325. https://doi.org/10.1039/c3nr01525d.

Kumar, A., Silotia, P., and Biradar, A.M. (2011). Sign reversal of dielectric anisotropy of ferroelectric liquid crystals doped with cadmium telluride quantum dots. Appl. Phys. Lett. *99*, 072902. https://doi.org/10.1063/1.3627179.

Lacková, V., Honecker, D., Kopčanský, P., and Tomašovičová, N. (2018). SANS Study of Magnetic Nanoparticles Ordering in Liquid Crystal Host (Institut Laue-Langevin (ILL)). https://doi.org/10.5291/ILL-DATA.9-11-1883.

Lagerwall, J.P.F., and Scalia, G. (2012). A new era for liquid crystal research: applications of liquid crystals in soft matter nano-, bio- and microtechnology. Curr. Appl. Phys. *12*, 1387–1412. https://doi.org/10.1016/j.cap.2012.03.019.

Li, T., Senesi, A.J., and Lee, B. (2016). Small angle X-ray scattering for nanoparticle research. Chem. Rev. *116*, 11128–11180. https://doi.org/10.1021/acs.chemrev.5b00690.

Liang, H.-H., Xiao, Y.-Z., Hsh, F.-J., Wu, C.-C., and Lee, J.-Y. (2010). Enhancing the electro-optical properties of ferroelectric liquid crystals by doping ferroelectric nanoparticles. Liq. Cryst. *37*, 255–261. https://doi.org/10.1080/02678290903564403.

Lorenz, A., Zimmermann, N., Kumar, S., Evans, D.R., Cook, G., and Kitzero, H.S. (2012). Doping the nematic liquid crystal 5CB with milled BaTiO. Phys. Rev. E *86*, 051704. https://doi.org/10.1103/PhysRevE.86.051704.

Mackert, V., Schroer and, M.A., and Winterer, M. (2021). Unraveling agglomeration and deagglomeration in aqueous colloidal dispersions of very small tin dioxide nanoparticles. J. Colloid Interf. Sci. https://doi.org/10.1016/j.jcis.2021.10.194.

Momin, N., Deshmukh, A., and Radha, S. (2015). Synthesis and characterization of $CnoFe^{2}o^{4}$-$NiFe^{2}O^{4}$ magnetic nanoparticles for various biomedical applications: cell viability and cell death evaluations. J. Nano Res. *34*, 1–8. https://doi.org/10.4028/www.scientific.net/JNanoR.34.1.

Patranabish, S., Wang, Y., Sinha, A., and Majundar, A. (2021). Quantum-dots-dispersed bent-core nematic liquid crystal and cybotactic clusters: experimental and theoretical insights. Phys. Rev. E *103*, 052703. https://doi.org/10.1103/PhysRevE.103.052703.

Petrov, M., Katranchev, B., Rafailov, P.M., Naradikian, H., Dettlaff-Weglikowska, U., and Keskinova, E. (2013). Smectic C liquid crystal growth and memory effect through surface orientation by carbon nanotubes. J. Mol. Liq. *180*, 215–220. https://doi.org/10.1016/j.molliq.2013.01.015.

Podoliak, N., Buchnev, O., Bavykin, D.V., Kulak, A.N., Kaczmarek, M., and Sluckin, T.J. (2012). Magnetite nanorod thermotropic liquid crystal colloids: synthesis, optics and theory. J. Colloid Interf. Sci. *386*, 158–166. https://doi.org/10.1016/j.jcis.2012.07.082.

Prakash, J., Khan, S., Chauhan, S., and Biradar, A.M. (2020). Metal oxide-nanoparticles and liquid crystal composites: a review of recent progress. J. Mol. Liq. *297*, 112052. https://doi.org/10.1016/j.molliq.2019.112052.

Prodanov, M.F., Buluy, O.G., Popova, E.V., Gamzaeva, S.A., Reznikov, Y.O., and Vashchenko, V.V. (2016). Magnetic actuation of a thermodynamically stable colloid of ferromagnetic nanoparticles in a liquid crystal. Soft Matter *12*, 6601–6609. https://doi.org/10.1039/c6sm00906a.

Qi, H., Kinkead, B., Marx, V.M., Zhang, H.R., and Hegmann, T. (2009). Miscibility and alignment effects of mixed monolayer cyanobiphenyl liquid-crystal-capped gold nanoparticles in nematic cyanobiphenyl liquid crystal hosts. ChemPhysChem *10*, 1211–1218. https://doi.org/10.1002/cphc.200800765.

Reshetnyak, V., Shelestiuk, S., and Sluckin, T. (2006). Fredericksz transition treshold in nematic liquid crystals filled with ferroelectric nanoparticles. Mol. Cryst. Liq. Cryst. *454*, 201–206. https://doi.org/10.1080/15421400600654108.

Rodarte, A.L., Gray, C., Hirst, L.S., and Ghosh, S. (2012). Spectral and polarization modulation of quantum dot emission in a one-dimensional liquid crystal photonic cavity. Phys. Rev. B *85*, 035430. https://doi.org/10.1103/PhysRevB.85.035430.

Rodarte, A.L., Nuno, Z.S., Cao, B.H., Pandolfi, R.J., Quint, M.T., Ghosh, S., Hein, J.E., and Hirst, L.S. (2014). Tuning quantum-dot organization in liquid crystals for robust photonic applications. ChemPhysChem *15*, 1413–1421. https://doi.org/10.1002/cphc.201301007.

Saari, M.M., Tsukamoto, Y., Kusaka, T., Ishihara, Y., Sakai, K., Kiwa, T., and Tsukada, K. (2015). Effect of diamagnetic contribution of water on harmonics distribution in a dilute solution of iron oxide nanoparticles measured using high-T_c SQUID magnetometer. J. Magn. Magn. Mater. *394*, 260–265. https://doi.org/10.1016/j.jmmm.2015.06.090.

Saliba, S., Mingotaud, C., Kahn, M.L., and Marty, J.D. (2013). Liquid crystalline thermotropic and lyotropic nanohybrids. Nanoscale *5*, 6641–6661. https://doi.org/10.1039/c3nr01175e.

Sanpo, N., Wang, J., and Berndt, C.C. (2013). Sol-gel synthesized copper-substituted cobalt ferrite nanoparticles for biomedical applications. J. Nano Res. *22*, 95–106. https://doi.org/10.4028/www.scientific.net/JNanoR.22.95.

Schroer, M.A., and Svergun, D.I. (2018). Recent developments in small-angle X-ray scattering and hybrid method approaches for biomacromolecular solutions. Emerg. Top. Life Sci. *2*, 69–79. https://doi.org/10.1042/ETLS20170138.

Schulz, F., Möller, J., Lehmkühler, F., Smith, A.J., Vossmeyer, T., Lange, H., Grübel, G., and Schroer, M.A. (2018). Structure and stability of PEG- and mixed PEG-layer coated nanoparticles at high particle concentrations studied in situ by small-angle X-ray scattering. Part. Part. Syst. Charact. *35*, 1700319. https://doi.org/10.1002/ppsc.201700319.

Sharifi, I., Shokrollahi, H., Doroodmand, M.M., and Safi, R. (2012). Magnetic and structural studies on $CoFe^{2}o^{4}$ nanoparticles synthesized by co-precipitation, normal micelles and reverse micelles methods. J. Magn. Magn. Mater. *324*, 1854–1861. https://doi.org/10.1016/j.jmmm.2012.01.015.

Silva, B.F.B., Zepeda-Rosales, M., Venkateswaran, N., Fletcher, B.J., Carster, L.G., Matsui, T., Weiss, T.M., Han, J., Li, Y., Olsson, U., et al. (2015). Nematic director reorientation at solid and liquid interfaces under flow: SAXS studies in a microfluidic device. Langmuir *31*, 4361–4371. https://doi.org/10.1021/la5034614.

Stamatoiu, O., Mirzaei, J., Feng, X., and Hegmann, T. (2012). Nanoparticles in liquid crystals and liquid crystalline nanoparticles. Top. Curr. Chem. *318*, 331–393. https://doi.org/10.1007/128_2011_233.

Svergun, D.I. (1992). Determination of the regularization parameter in indirect-transform methods using perceptual criteria. J. Appl. Cryst. *5*, 495–503. https://doi.org/10.1107/S0021889892001663.

Svergun, D.I. (1999). Restoring low resolution structure of biological macromolecules from solution scattering using simulated annealing. Biophys. J. *76*, 2879–2886. https://doi.org/10.1016/S0006-3495(99)77443-6.

Svergun, D.I., Koch, M.H.J., Timmins, P.A., and May, R.P. (2013). Small Angle X-Ray and Neutron Scattering from Solutions of Biological Macromolecules (Oxford University Press).

Tóth-Katona, T., Salamon, P., Éber, N., Tomašovičová, N., Mitróová, Z., and Kopčanský, P. (2014). High concentration ferronematics in low magnetic fields. J. Magn. Magn. Mater. *372*, 117–121. https://doi.org/10.1016/j.jmmm.2014.07.061.

Zákutná, D., Nižňanský, D., Barnsley, L.C., Babcock, E., Salhi, Z., Feoktysov, A., Honecker, D., and Disch, S. (2020). Field dependence of magnetic disorder in nanoparticles. Phys. Rev. X *10*, 031019. https://doi.org/10.1103/PhysRevX.10.031019.

STAR★METHODS

KEY RESOURCES TABLE

REAGENTor RESOURCE	SOURCE	IDENTIFIER
Chemicals		
16-Bromohexadecanoic acid (≥99%)	Sigma-Aldrich	CAS: 2536-35-8
NaH (suspension 60% in paraffin oil)	Sigma-Aldrich	CAS: 7646-69-7
Tetrabutylammonium hydrogen sulfate (97%)	Alfa Aeser	CAS: 32,503-27-8
4-Cyano-4′-pentylbiphenyl (99%),	Alfa Aeser	CAS: 40,817-08-1
4-Hydroxy-4-biphenylcarbonitrile (99%)	Alfa Aeser	CAS: 19,812-93-2
Iron(III)chloride (reagent grade)	Sigma-Aldrich	CAS: 7705-08-0
Cobalt(II)chloride hexahydrate (≥99%)	Carl Roth	CAS: 7791-13-1
Software and algorithms		
SAXS: ATSAS software	https://www.embl-hamburg.de/biosaxs/software.html	Version 3.0.3
MATLAB	MathWorks	Version R2019a

RESOURCE AVAILABILITY

Lead contact

Further information and requests for resources and reagents should be directed to and will be fulfilled by the lead contact, Natália Tomašovičová (nhudak@saske.sk).

Materials availability

Materials may be provided upon reasonable request for a specific purpose.

Data and code availability

- The published article includes all data analyzed during this study.
- No original code was generated in the present study.
- Any additional information required to reanalyze the data reported in this paper is available from the lead contact upon request.

METHOD DETAILS

Synthesis of electrostatically stabilized CFO-MNPs

Electrostatically stabilized $Co_xFe_{3-x}O_4$ MNPs were synthesized following a modified procedure (Appel et al., 2017). Briefly, a mixture of $FeCl_3$ (2 mL, 2 M in water) and $CoCl_2$ (1 mL, 2 M in 3 M hydrochloric acid) was injected (~1 s) into a NaOH solution (80 mL, 1 M) at 50°C while stirring. Then, the reaction mixture was heated to 100°C (heating rate ~5°C/min). After 30 min the MNPs were collected by centrifugation and washed three-times with water. Then, perchloric acid (5 mL, 1 M in water) was added and aggregates were removed by centrifugation to give MNPs as an electrostatically stabilized brown-black colloidal suspension. The composition of the MNPs was determined as $Co_xFe_{3-x}O_4$ (x = 0.6) by atomic emission spectrometry with inductively coupled plasma (ICP-OES). The particle size was determined by transmision electron microscopy (TEM). For this purpose, N = 300 MNPs were accounted with an average particle size for the magnetic core of d = 3.1 (±0.8) nm.

Synthesis of CFO@ligand-MNPs *via* direct functionalization

First, the (pro)mesogenic ligand [16-((4′-cyano-[1,1′-biphenyl]-4-yl)oxy)hexadecanoic acid] was synthesized (Appel et al., 2017). Then, the (pro)mesogenic ligand (200 mg, 0.4 mmol) was dissolved in anhydrous dimethylformamide (30 mL) at 40°C. The MNPs (830 μL MNPs in 1 M perchloric acid) were added and the reaction mixture was stirred at 60°C. After 3.5 h, CFO@ligand-MNPs were precipitated by addition of EtOH (20 mL), washed with EtOH (3 × 20 mL) and eventually magnetically separated.

Preparation of FN mixtures: Doping 5CB with CFO@ligand-MNPs

The CFO@ligand-MNPs were dispersed in 5CB (10 mL) with an ultrasonic probe at 40°C. After transition to the nematic phase, macroscopic precipitates were removed by magnetic separation (25°C, 16 h). A colloidal stable suspension was obtained with 0.131 wt.% CFO in 5CB. The FN mixture was diluted with 5CB to prepare a series of five samples with different CFO@ligand-MNPs concentration: LC1) 0.065 wt.%; LC2) 0.082 wt.%; LC3) 0.098 wt.%; LC4) 0.115 wt.% and LC5) 0.131 wt.% (stock solution).

Magnetisation measurements

The magnetic properties of the 5CB and FNs mixtures were measured using an SQUID magnetometer (Quantum Design MPMS 5XL). The samples were filled into cylindrical capsules, which were hermetically closed. The diameter of the capsules was 2.5 mm and length was 6.5 mm. A diamagnetic signal coming from the container was subtracted after each measurement. The measurement of magnetisation curves was performed at 295 K (~22°C) in the nematic phase.

Small angle X-ray scattering

Small angle X-ray scattering (SAXS) measurements were performed at the BioSAXS beamline P12, EMBL/DESY, Hamburg, Germany (Blanchet et al., 2015), using the 150 μm (V) × 250 μm (H) X-ray beam with an energy of $E = 10$ keV (wavelength $\lambda = 0.124$ nm). Two-dimensional SAXS patterns were recorded using a Pilatus 6M pixel detector (Kraft et al., 2009), at a sample-detector-distance of 3 m, covering the range of momentum transfer q = 0.04–7.3 nm^{-1} ($q = 4\pi/\lambda\sin(\theta)$, where 2θ is the scattering angle). The samples were filled into quartz glass capillaries (Hilgenberg, Germany; outer diameter: 1.50 mm, wall thickness: 0.01 mm) and placed within a custom-made temperature controlled capillary holder with a Peltier element. Temperature-dependent measurements were performed in the range from $T = 20$°C to 40°C with 1°C step to monitor the thermally driven transition from the nematic to the isotropic phase of the FNs. Afterward, samples were cooled down back to 20°C. For the samples within the isotropic phase, there is no preferred orientation and the SAXS patterns were azimuthally averaged and normalized by the P12 beamline SASFLOW pipeline (Franke et al., 2012). From these 1D-SAXS curves the background signal from water was subtracted and the difference profiles were further analyzed using the ATSAS software package (Franke et al., 2017).

Small angle neutron scattering

Magnetic-field dependent small-angle neutron scattering (SANS) were performed on D33 at the Institut Laue-Langevin, Grenoble, France (Lacková et al., 2018; Dewhurst et al., 2016) using a neutron wavelength of 3.5 Å(dλ/λ = 15%). The two-dimensional SANS was recorded for two instrument configurations with sample-to-detector distances of 2 m and 12.8 m and similar collimation setting (2.8 m and 12.8 m), respectively, which allowed to cover a range of q comparable to the SAXS measurements (0.08–6.2 nm^{-1}) (Lacková et al., 2018). The rear detector captures the data at small momentum transfer q, while the scattering at extended high q were accessible with the surrounding panels of the front detector on D33. A gap in q-coverage around 3 nm^{-1} occurs due to a lateral offset of the panels from the main detector (Dewhurst et al., 2016). The samples were filled in rectangular quartz cells with a path length of 2 mm and placed inside an electromagnet, which provided a magnetic field of up to 1 T. Finally, all measurements have been performed at temperature of 25°C.

Dielectric measurements

Structural transitions of FNs were monitored by capacitance measurements, where samples were introduced by capillary action into about D = 50 μm thick sandwich cells (MUT, Poland) (0.5 cm × 0.5 cm) made of indium-tin-oxide (ITO) coated glass electrode. The initial alignment of LC molecules was planar, i.e. the director $\vec{n}$ was parallel to the capacitor electrodes. The capacitor has been placed into a thermostat system, regulated with the temperature stability of 0.05°C, and the measurements have been done at the temperature of 30°C. The capacitance C was measured at the frequency of 1 kHz by a high precision capacitance bridge (Andeen Hagerling, USA) with an accuracy of 0.8 aF at 1 kHz. The magnetic field was applied perpendicular with the initial director orientation $\vec{n}$. In this geometry, the magnetic field destabilizes the initial director orientation. Therefore, it is possible to determine the threshold behavior in the reorientational response of LCs or FNs.